

Shortest Microlensing Event with a Bound Planet: KMT-2016-BLG-2605

YOON-HYUN RYU¹, KYU-HA HWANG¹, ANDREW GOULD^{2,3}, JENNIFER C. YEE⁴,
MICHAEL D. ALBROW⁵, SUN-JU CHUNG^{1,6}, CHEONGHO HAN⁷, YOUN KIL JUNG¹,
HYOUN-WOO KIM^{1,8}, IN-GU SHIN¹, YOSSI SHVARTZVALD⁹, WEICHENG ZANG¹⁰,
SANG-MOK CHA^{1,11}, DONG-JIN KIM¹, SEUNG-LEE KIM^{1,6}, CHUNG-UK LEE^{1,6},
DONG-JOO LEE¹, YONGSEOK LEE^{1,11}, BYEONG-GON PARK^{1,6}, RICHARD W. POGGE³

¹*Korea Astronomy and Space Science Institute, Daejeon 34055, Republic of Korea*

²*Max-Planck-Institute for Astronomy, Königstuhl 17, D-69117 Heidelberg, Germany*

³*Department of Astronomy, Ohio State University, 140 W. 18th Ave., Columbus, OH
43210, USA*

⁴*Center for Astrophysics | Harvard & Smithsonian, 60 Garden St., Cambridge, MA 02138,
USA*

⁴*Department of Astronomy and Space Science, Chungbuk National University, Cheongju
28644, Republic of Korea*

⁵*University of Canterbury, Department of Physics and Astronomy, Private Bag 4800,
Christchurch 8020, New Zealand*

⁶*Korea University of Science and Technology, Korea, (UST), 217 Gajeong-ro, Yuseong-gu,
Daejeon, 34113, Republic of Korea*

⁷*Department of Physics, Chungbuk National University, Cheongju 28644, Republic of Korea*

⁸*Department of Astronomy and Space Science, Chungbuk National University, Cheongju
28644, Republic of Korea*

⁹*Department of Particle Physics and Astrophysics, Weizmann Institute of Science, Rehovot
76100, Israel*

¹⁰*Physics Department and Tsinghua Centre for Astrophysics, Tsinghua University, Beijing
100084, China*

¹¹*School of Space Research, Kyung Hee University, Yongin, Kyeonggi 17104, Republic of
Korea*

ABSTRACT

KMT-2016-BLG-2605, with planet-host mass ratio $q = 0.012 \pm 0.001$, has the shortest Einstein timescale, $t_E = 3.41 \pm 0.13$ days, of any planetary microlensing event to date. This prompts us to examine the full sample of 7 short ($t_E < 7$ day) planetary events with good q measurements. We find that six have clustered Einstein radii $\theta_E = 115 \pm 20 \mu\text{as}$ and lens-source relative proper motions $\mu_{\text{rel}} \simeq 9.5 \pm 2.5 \text{ mas yr}^{-1}$. For the seventh, these two quantities could not be measured. These distributions are consistent with a Galactic-bulge population of very low-mass (VLM) hosts near the hydrogen-burning limit. This conjecture could be verified by imaging at first adaptive-optics light on next-generation (30m) telescopes. Based on a preliminary assessment of the sample, “planetary” companions (i.e., below the deuterium-burning limit) are divided into “genuine planets”, formed in their disks by core accretion, and very low-mass brown dwarfs, which form like stars. We discuss techniques for expanding the sample, which include taking account of the peculiar “anomaly dominated” morphology of the KMT-2016-BLG-2605 light curve.

Subject headings: gravitational lensing: micro

1. Introduction

Microlensing planets are almost always discovered from short-lived perturbations on otherwise single-lens single-source (1L1S) bell-shaped Paczyński (1986) light curves, as predicted by (Mao & Paczyński 1991), Gould & Loeb (1992), and Griest & Safizadeh (1998). However, there are occasional exceptions.

If the planet-host mass ratio q is relatively large and the lens-source separation (normalized to the Einstein radius, θ_E) is close to unity, $s \sim 1$, then the central and planetary caustics merge into a single, large, resonant caustic, which can induce a long-term anomaly over the peak of the event. For example, the $q = 10^{-2}$ event MOA-2009-BLG-387 (Batista et al. 2011) showed strong, continuous anomalies over 9 days. Nevertheless, over the remainder of the $2t_E \sim 80$ days of the event, it appeared as qualitatively normal. And, indeed, it is on the basis of this normal rising behavior that the Microlensing Follow Up Network (μFUN) initiated followup observations two days before the anomaly. Here, t_E is the Einstein timescale.

A very different counter-example, in this case a “purely anomalous event” is given by MOA-bin-1 (Bennett et al. 2012), for which the entire observed event consists of the source crossing the planetary caustic. Because the planet-host separation is $s \sim 2$ and the source trajectory is nearly perpendicular to the planet-host axis, $\alpha \sim 90^\circ$, the $t_E \sim 31$ day “host

event” leaves barely a trace on the light curve. Thus, essentially all that remains is the short, ~ 0.2 day triangular anomaly due to the $q \sim 5 \times 10^{-3}$ planet.

Here we present another rare case for which the light curve is dominated by a planet-induced anomaly, KMT-2016-BLG-2605. Like MOA-2009-BLG-387, the anomaly is due to a resonant caustic of a $q \sim 10^{-2}$ planet. And like MOA-bin-1, the duration of the anomaly is short (1.5 days). Indeed, the observed portion of the anomaly is only ~ 0.5 days. However, in contrast to either of these cases, the underlying timescale is very short, $t_E = 3.4$ days, while the microlensed source is faint, $I_s = 20.2$, so that only the anomaly is really noticeable, particularly in the initial reductions from which the event was discovered. For this reason, the event was not discovered in the original search carried out by the Korean Microlensing Telescope Network (KMTNet, Kim et al. 2016) EventFinder system (Kim et al. 2018a), during which it was misclassified as a cataclysmic variable (CV). It was recognized as genuine microlensing only as a byproduct of a special search that was conducted for another purpose (Kim et al. 2020).

KMT-2016-BLG-2605 is one of only seven short-timescale ($t_E < 7$ day) planetary events with a well measured mass ratio q (less than factor 2 difference between competing solutions at $\Delta\chi^2 < 10$). The roughly comparable properties of this ensemble ($\theta_E \sim 0.11$ mas, $\mu_{\text{rel}} \sim 9$ mas yr $^{-1}$, where μ_{rel} is the lens-source relative proper motion) are consistent with a population of Galactic-bulge hosts that have masses near the hydrogen-burning limit. For six of these seven (including KMT-2016-BLG-2605), this assessment can be confirmed or contradicted at first adaptive-optics (AO) light on next-generation (30m class) telescopes.

Despite the fact that all seven were detected through resonant or near-resonant caustics, KMT-2016-BLG-2605 is the only anomaly-dominated event, which would potentially make it more difficult to recognize during the manual stage of event selection. We consider this and other factors to evaluate the challenges in identifying more of these short- t_E planetary systems.

2. Event Identification

KMT-2016-BLG-2605 was identified as a “clear” microlensing event during a special search of the 2016 KMTNet data that was conducted as part of a project to identify all finite-source point-lens (FSPL) giant-source events during the four year span 2016-2019. The primary objective of this project is to create a statistically well defined parent sample that will contain a free-floating planet (FFP) subsample. A special additional search was found to be necessary because a significant fraction of short FSPL events were missed by

the primary EventFinder (Kim et al. 2018a) searches that are done annually. For example, some giant-star sources had been eliminated from the search because of previously cataloged variability, or light-curve artifacts. Of course, it is known that variable stars can undergo microlensing events that can be distinguished from their intrinsic variations, and also that many light-curve artifacts do not repeat from year to year. However, the fraction of real events that are removed this way is small ($\sim 1\%$), while the human cost of manual review is high. Thus, removal of these sources from the regular search is a rational approach. Nevertheless, when the search is restricted to giant sources, the cost is reduced by a factor of about 20, making lifting (or strongly modifying) these criteria worthwhile for the FSPL project.

Another feature of the special search was that the candidates selected by the machine algorithm were shown to the operator in several additional displays. This is because the shortest FSPL events can be highly anomalous due to finite source effects. Thus, when the three data sets are automatically aligned using Paczyński (1986) or Gould (1996) fits, the joint light curve can appear to be “clearly not microlensing”. By having multiple displays, by having the operator spend more time reviewing each candidate, and by adopting somewhat lower standards on what is a plausible microlensing event, it is much less likely that these short FSPL events will be rejected at this stage. Of course, non-microlensing events can still be rejected at a later stage when each candidate is manually fit to point-source point-lens (PSPL) and FSPL functional forms. For more details on these special searches, see Kim et al. (2020) and Ryu et al. (2021).

The special search for 2016 identified 281 candidates, of which 37 had not been found in the regular EventFinder search¹. KMT-2016-BLG-2605 was number 17 on this list of 37 new candidates. Following the convention of Mróz et al. (2020) and Ryu et al. (2021), it was assigned the sequential label “2605” ($= 2588 + 17$) because there were 2588 events discovered in the original search.

KMT-2016-BLG-2605 is neither an FSPL event nor does it have a giant-star source. Nevertheless, it passed the various selection criteria imposed to obtain a sample of just seven new events² from 2016 that would then be subjected to manual FSPL fitting. The machine search of the KMTNet database is restricted to “giant” source stars, defined as having dereddened baseline magnitudes $I_{\text{base},0} = I_{\text{cat}} - A_I < 16.2$, where I_{cat} is the magnitude of the catalog entry, $A_I = A_K/7$, and A_K is derived from Groenewegen (2004). This led

¹Of these 37, 10 had previously been identified by other teams, including seven by OGLE, two by MOA and one by both.

²Two of these seven proved to be FSPL events.

to $I_{\text{base},0} = 18.63 - 2.74 = 15.89$. Being a very short event, it then easily passed the machine-search criterion that the effective timescale be less than 5 days. When it was displayed to the operator, it did not look like 1L1S microlensing (neither PSPL nor FSPL), but at this stage the only criterion is that the variation is plausibly due to microlensing. As described by Kim et al. (2020), all events (including these 37 from the 2016 special search) are selected for manual review by two criteria. The first is $I_{s,0} = I_s - A_I < 16$, where I_s is the source magnitude from the pipeline fit to the event. As we will show in Section 4, the true value of $I_{s,\text{kmt}} = 20.0$, for which case $I_{s,0} = 17.3$, i.e., failing this criterion by more than a magnitude. Nevertheless, due to the extremely anomalous form of the light curve, the pipeline fit assigned $I_s \rightarrow I_{\text{cat}}$, which allowed the event to pass this criterion. Second, it easily passed the criterion meant to select plausibly FSPL (as opposed to almost certainly PSPL) events, $\mu_{\text{thresh}} = 3 \text{ mas } 10^{(16-I_{s,0})/5} / u_0 t_E > 1 \text{ mas yr}^{-1}$, where u_0 is the impact parameter (normalized to θ_E) of the pipeline fit. Given that $u_0 t_E = 0.147 \times 1.59 \text{ day} = 5.6 \text{ hr}$, it had $\mu_{\text{thresh}} = 5 \text{ mas yr}^{-1}$.

It was only in the course of fitting the event to 1L1S models by hand that it became clear that the slope of the light curve showed a discontinuous change at $\text{HJD}' = \text{HJD} - 2450000 = 7565.3$, indicating a caustic crossing, which could plausibly be explained by a planetary system.

In brief, KMT-2016-BLG-2605 came to our attention by a most unlikely and circuitous path, a point to which we will return in Section 7. For example, if the source star were not blended with another star that was several times brighter, it would not have even been selected for machine fitting at the first step.

3. Observations

KMT-2016-BLG-2605 is at equatorial coordinates $(\text{R.A.}, \text{Decl})_{J2000} = (17:59:17.54, -26:58:55.20)$, corresponding to galactic coordinates $(l, b) = (+3.22, -1.60)$. It therefore lies in KMTNet field BLG03. KMTNet consists of three 1.6m telescopes, each equipped with a 4 deg² camera, and located in Chile (KMTC), South Africa (KMTS), and Australia (KMTA). At the time of the event, BLG03 was observed with a cadence $\Gamma = 2 \text{ hr}^{-1}$ from each observatory, primarily in the I band. In 2016, every tenth I -band observation at KMTC was complemented by one in the V band, as was every twentieth observation at KMTS. There were no V -band observations from KMTA³.

³Based on experience with OGLE-2015-BLG-1459 (Hwang et al. 2019), it was realized that KMTA V -band observations were potentially very important, and ultimately both KMTS and KMTA were observed

The data were initially reduced using pySIS (Albrow et al. 2009), which is a specific implementation of difference image analysis (Tomaney & Crotts 1996; Alard & Lupton 1998). Moreover, the original light-curve analysis was based on tender loving care (TLC) pySIS re-reductions. However, as we describe in Section 4, it was ultimately necessary to use a related package, pyDIA (Albrow 2017) because it returns field-star photometry on the same system as the light curve. To avoid confusion, we present the entire investigation of the light curve using pyDIA photometry.

4. Light Curve Analysis

We fit the data to binary-lens single-source (2L1S) models, which are characterized by seven parameters $(t_0, u_0, t_E, s, q, \alpha, \rho)$, where t_0 is the time of closest lens-source approach and $\rho = \theta_*/\theta_E$ is the source radius normalized to the Einstein radius. As is almost always done, we begin with a grid search over an (s, q, α) grid, in which (s, q) are held fixed and $(t_0, u_0, t_E, \alpha, \rho)$ are allowed to vary in a Monte Carlo Markov chain (MCMC). The three Paczyński (1986) parameters (t_0, u_0, t_E) are seeded at the PSPL fit, while ρ is seeded at $\rho = 0.003$.

However, in contrast to typical experience, we find a plethora of quite distinct solutions. After refitting each local minimum of the grid with all seven parameters allowed to vary, we find seven distinct solutions within the range of $\Delta\chi^2 < 100$. However, only Locals 1–3 are potentially viable, with $\Delta\chi^2 < 11$, while Locals 4–7 have $\Delta\chi^2 > 50$. Closer examination of Local 1 shows that it breaks up into three nearby minima. See Table 1. Figure 1 shows the models and data for the three principal Locals, while Figure 2 shows the principal Local 1 and its two satellite solutions.

Comparing Locals 1 and 1b in Figure 2, we see that the peak of the former (specifically, the second KMTS point at $\text{HJD}' = 7565.28$) is 0.25 mag fainter. This is unusual for competing microlensing solutions. When presenting microlensing models, one data set (in this case, KMTS) is chosen as the “anchor”. Its data values are exactly reproduced in the figure. All other data sets are aligned, by linear regression of the fluxes to the model, to this anchor. Because this alignment is usually based on several nights of data during which the event is evolving in a regular way, the alignment coefficients are normally the same for different models. Hence, the different data sets are rigidly aligned to the same fiducial scale, independent of model. For this reason, all models can be shown by curves that are superposed on data points whose positions are fixed.

in the I and V bands at a ratio of 10 : 1. Unfortunately, this was not the case in 2016.

However, in the present case, the KMTS and KMTA data are strongly magnified on only one night. Hence the alignment is not fully constrained by other nights. The lack of a rigid constraints is reflected in the range of values in the quantity $\Delta I = I_{S,,kmts} - I_{S,kmtc}$ that is shown in Table 1.

At most one of these ΔI values can be correct. That is, these offsets represent the relative transparency and throughput of the detectors at the two sites. And this quantity can be measured from field stars (Gould et al. 2010; Yee et al. 2012).

To make this comparison precise, we have carried out the MCMCs with the source-flux and blend-flux parameters from each observatory treated as chain variables, That is, normally one writes

$$F_i(t_{i,j}) = f_{s,i}A(t_{i,j}; t_0, u_u, t_E, s, q, \alpha, \rho) + f_{b,i} , \quad (1)$$

where $F_i(t)$ is the observed flux from observatory i at time t , and $(f_{s,i}, f_{b,i})$ are the source-flux and blend-flux parameters for observatory i . At each step on the MCMC, one inserts the trial values for the seven parameters $(t_0, u_u, t_E, s, q, \alpha, \rho)$, but one determines $(f_{s,i}, f_{b,i})$ from a linear fit to the model magnifications A . For the vast majority of cases, the errors that would be induced in these parameters due to the flux errors at a given model is tiny compared their error due to variation between different models. Hence, this approach is usually appropriate.

However, for the present case, the value of $f_{s,kmtc}$ is basically determined by just 16 data points on the night after the peak. These individually have fractional scatter $\sigma(F)/[(A - 1)f_s \sim 0.075$, which implies that the standard error of the mean should be of order $(2.5/\ln 10) \times 0.075/\sqrt{16} \sim 0.02$ mag. This is too large to be ignored in the present context. Hence, we also treat f_s and f_b as chain parameters.

Finally, we match the field-star photometry of the KMTS03 and KMTA03 reductions, and we plot the differences as a function of magnitude in Figure 3. For this purpose, we only include stars with $(V - I)_{kmts} > 3.0$, which includes the colors of the source and the red clump. We plot the predicted offsets from the five models as horizontal lines with error ranges.

We see that $(I_{s,kmts} - I_{s,kmtc})_{Local-1}$ is consistent with the field stars at 1σ , whereas $(I_{s,kmts} - I_{s,kmtc})$ is inconsistent at $\geq 2.3\sigma$ for all the other solutions. Keeping in mind that Local 1 was already favored over Locals 2 and 3 by $\Delta\chi^2 \gtrsim 10$ (and by slightly less compared to its satellite solutions), we regard this as clear confirmation of Local 1.

Finally, we impose the flux constraint within the MCMC as a χ^2 penalty,

$$\chi_{\text{flux}}^2 = \left(\frac{-2.5 \log(f_{S,kmts}/f_{S,kmtc}) - -0.033}{0.005} \right)^2 . \quad (2)$$

We find that Locals 1a and 1b disappear as separate minima, while Locals 2 and 3 are each disfavored by $\Delta\chi^2 \sim 16$. See Table 2. We adopt the Local 1 microlensing parameters in this table as our final result. Figure 4 shows the best-fit model and data after imposing this constraint. It also shows the caustic topology, which is resonant.

5. Source Properties

As with most other microlensing events, we measure θ_* using the method of Yoo et al. (2004). This requires that we first find the offset $\Delta[(V-I), I] = [(V-I), I]_s - [(V-I), I]_{cl}$ of the source star relative to the clump. Adopting $[(V-I), I]_{cl,0} = (1.06, 14.34)$ (Bensby et al. 2013; Nataf et al. 2013), we would then derive the dereddened source color and magnitude, $[(V-I), I]_{s,0} = \Delta[(V-I), I] + [(V-I), I]_{cl,0}$, convert from V/I to V/K photometry using the VIK color-color relations of Bessell & Brett (1988), and finally, use the color/surface-brightness relation of Kervella et al. (2004) to derive the angular radius of the source star, θ_* .

Unfortunately, the first step in this procedure, determining $\Delta[(V-I), I]$, poses substantially greater challenges for KMT-2016-BLG-2605 than it does for typical events because the color-magnitude diagram (CMD) positions of both the source star and the clump are more difficult to determine.

In the Appendix, we delineate the steps to measure the clump position, which we show is well determined. However, we show that while the source magnitude is also well determined, the source color remains somewhat ambiguous. The key issue is that the source color derived from the light curve, which rests on a single magnified V -band data point, is in formal conflict with Bayesian expectations based on the well-determined magnitude (together with the morphology of the CMD). After weighing all the evidence, we conclude that, most likely, the discrepancy is due to a relatively large ($\lesssim 3\sigma$) statistical error in the single V -band data point, and we adopt

$$(V-I)_{s,0} = 1.00 \pm 0.05 \quad (3)$$

Then, following the steps outlined in the first paragraph of this section, we find

$$\theta_* = 1.38 \pm 0.10 \mu\text{as}, \quad (4)$$

where we have added 5% in quadrature to the error bar to take account of systematics that are inherent to the method. From this we then derive,

$$\theta_E = \frac{\theta_*}{\rho} = 0.116 \pm 0.009 \text{ mas}; \quad \mu_{\text{rel}} = \frac{\theta_*}{t_*} = 12.3 \pm 1.0 \text{ mas yr}^{-1}, \quad (5)$$

where $t_* \equiv \rho t_E$.

However, in the Appendix, we also keep track of the possibility that the light-curve color measurement is actually correct, in which case, $\theta_* = 1.77 \pm 0.23 \mu\text{as}$, $\theta_E = 1.49 \pm 0.19 \text{mas}$, and $\mu_{\text{rel}} = 15.8 \pm 1.3 \text{mas yr}^{-1}$.

6. Physical Parameters

We make a standard Bayesian analysis to derive physical parameters. That is, we draw events randomly from a Galactic model, and we weight each simulated event by how well it conforms to Equation (5). We additionally weight by the event rate, $\Gamma \propto \theta_E \mu_{\text{rel}}$, although this has very little effect because these parameters are very similar for all simulated events that satisfy Equation (5). The Galactic model follows that of Jung et al. (2018a) as modified by Jung et al. (2021). The results are reported in Table 4, and they are illustrated in Figure 5, which shows that the lens probably lies in the bulge, but even if not, it most likely lies in overlapping regions of the disk. The median host mass estimate, $M_{\text{host}} = 0.064_{-0.032}^{+0.099}$ is very close to the hydrogen-burning limit, i.e., there is a roughly 50% probability that it is a brown dwarf (BD). If we adopt a snow-line scaling $a_{\text{snow}} = 2.7 \text{AU} (M_{\text{host}}/M_{\odot})$, then the planets projected separation is $a_{\perp} \sim 4 a_{\text{snow}}$.

Kim et al. (2021) have shown that, unless $\mu_{\text{rel}} > 10 \text{mas yr}^{-1}$ (or there is additional information such as a microlens parallax measurement), the Bayesian mass estimate depends only on θ_E . While this condition does not apply to KMT-2016-BLG-2605, if we nevertheless input $\theta_E = 0.116 \text{mas}$ into their Figures 7, we obtain $M = 0.08_{-0.04}^{+0.06} M_{\odot}$. The difference between this and our Bayesian estimate is accounted for by the “bend” in the median trajectories above $\mu = 10 \text{mas yr}^{-1}$ in their Figure 6.

7. Discussion

7.1. Ensemble of Short-timescale Planets

At $t_E = 3.41 \text{days}$, KMT-2016-BLG-2605 has the shortest timescale of any planetary microlensing event. There are eight previous binary-lens microlensing events with $3.7 < t_E/\text{day} < 7$ that are listed by the NASA Exoplanet Archive⁴. For the present discussion,

⁴<https://exoplanetarchive.ipac.caltech.edu/>. We chose “7 days” as the upper limit, without foreknowledge of the sample that it would produce, because 7 is the closest integer to $2 \times t_E/\text{day}$ of KMT-2016-BLG-2605.

we restrict attention to the subset with (1) unambiguous measurement of q (specifically, no solutions with $\Delta\chi^2 < 10$ and q values differing by a factor > 2); and (2) “verifiable planet”, specifically $q < M_{\text{D-burn}}/M_{\text{H-burn}} = 0.16$. That is, we accept the formal definition of a “planet” as having mass m_p below the deuterium burning limit, $m_p < M_{\text{D-burn}}$. Systems with q above this limit can be ruled out as planets if their hosts are stars $M_{\text{host}} > M_{\text{H-burn}}$ because these can be imaged at late times. But a non-detection would leave the status of the companion ambiguous. However, for systems satisfying this condition, even a non-detection would prove the companion had planetary mass. Two events fail criterion (1): MOA-bin-29 (Kondo et al. 2019) and MOA-2015-BLG-337 (Miyazaki et al. 2018). One event fails criterion (2): KMT-2016-BLG-2124 (Jung et al. 2018b).

The remaining five events are MOA-2011-BLG-262 (Bennett et al. 2014), OGLE-2015-BLG-1771 (Zhang et al. 2020), KMT-2018-BLG-0748 (Han et al. 2020), OGLE-2018-BLG-0677 (Herrera-Martin et al. 2020), and KMT-2016-BLG-1820 (Jung et al. 2018b). We note that, strictly speaking, the first of these events has an ambiguous measurement of ρ , i.e., $\rho = 3.44 \times 10^{-3}$ or $\rho = 5.73 \times 10^{-3}$, with the first preferred by $\Delta\chi^2 = 3$. However, the first solution would imply a geocentric proper motion⁵ $\mu_{\text{rel}} = 21.6 \pm 2.3 \text{ mas yr}^{-1}$. As the authors note, their OGLE-III-based measurement of the source proper motion $\boldsymbol{\mu}_s(l, b) \sim (-2.4, -0.4) \pm (2.7, 2.7) \text{ mas yr}^{-1}$ implies that the high proper-motion solution is inconsistent with bulge lenses. It would imply that the lens must lie far in the foreground, e.g., at $D_L \lesssim 1 \text{ kpc}$. In this case, the host mass would be $M \lesssim 6 M_J$, with “planet” (aka “moon”) mass $m \lesssim 0.9 M_{\oplus}$. The “novelty” of this putative system, combined with the small number of potential lenses in the nearby observational cone, renders this solution highly unlikely. Therefore, for this purpose, we adopt the higher- ρ solution.

To this sample, we add KMT-BLG-2019-BLG-0371 (Kim et al. 2021), which is not listed at NASA Exoplanet Archive because it has not yet been accepted for publication.

Table 3 shows the observed characteristics of the six previous systems⁶, together with those of KMT-2016-BLG-2605. Excluding for the moment OGLE-2018-BLG-0677 (for which ρ is not measured), the remaining six events all have Einstein radii θ_E in the range $115 \pm 20 \mu\text{as}$, and three have proper motions $\mu_{\text{rel}} \sim 9.5 \text{ mas yr}^{-1}$, with the other three deviating by $2\text{--}3 \text{ mas yr}^{-1}$.

These characteristics are consistent with expectations for a population of planet-bearing

⁵The authors quote $19.6 \pm 1.6 \text{ mas yr}^{-1}$, which may reflect a posterior result after applying unstated Bayesian priors.

⁶The values in this table have been somewhat compressed and simplified in order to aid visual assimilation of the patterns. The reader should consult the original papers for the exact parameter values and error bars.

hosts near the star-BD boundary and lying in the Galactic bulge. That is, the total mass of these systems (dominated by the host) is given by

$$M = \frac{\theta_E^2}{\kappa\pi_{\text{rel}}} = 0.10 M_\odot \left(\frac{\theta_E}{115 \mu\text{as}} \right)^2 \left(\frac{\pi_{\text{rel}}}{16 \mu\text{as}} \right)^{-1}; \quad \kappa \equiv \frac{4G}{c^2 \text{AU}} \simeq 8.14 \frac{\text{mas}}{M_\odot}, \quad (6)$$

where we have scaled to a typical relative parallax, $\pi_{\text{rel}} = 16 \mu\text{as}$, for bulge-bulge microlensing. Under conditions that the “mass function” (i.e., in this case, the mass function of stars/BDs that host planets) has a “hard floor”, the shortest-timescale events will be generated by systems near this floor, and with source-lens separations D_{LS} near the “edge” of the bulge distribution. In fact, there is no real “edge”, but there is a rapid fall-off. It is also unlikely that there a “hard floor” to the mass function, but it is plausible that there is, again, a rapid fall-off.

The same picture naturally explains the high proper motions. For an isotropic proper-motion distribution with Gaussian width $\sigma = 2.9 \text{mas yr}^{-1}$ (which approximately characterizes the bulge), the mean and standard deviation of the lens-source relative proper motion is (Gould et al. 2021a),

$$\mu_{\text{rel}} = \left(\frac{4}{\sqrt{\pi}} \pm \sqrt{6 - \frac{16}{\pi}} \right) \sigma \rightarrow 6.5 \pm 2.8 \text{mas yr}^{-1}. \quad (7)$$

Thus, we expect that if there is a “floor” on the mass function (whether “hard” or “soft”), the proper motions of the shortest events will tend toward the upper range where the distribution is falling off rapidly, roughly 1σ above the mean, which is 9.3mas yr^{-1} in the present case.

These are just plausibility arguments, and no more is really possible at this point because of the inhomogeneous selection of the sample. However, it will be straightforward to test this conjecture by imaging the systems at first AO light on next-generation (30m class) telescopes, in roughly 2030. In all cases, the sources are dwarf stars, turnoff stars or subgiants, and hence have $M_K \gtrsim 2$, compared to $M_K \sim 10$ of stars at the bottom of the main sequence, i.e., contrast ratios of $\lesssim 8$ magnitudes. Bowler et al. (2017) achieved contrast ratios of (5, 10) magnitudes at separation $\Delta\theta \sim (150, 320)$ mas using AO on the Keck 10m telescope. Scaling to 25m (for the Giant Magellan Telescope, GMT) to 30m (for the Thirty Meter Telescope, TMT), and to 39m (for the European Extremely Large Telescope, EELT), these correspond to $\Delta\theta \sim (60, 130)$ mas, $\Delta\theta \sim (50, 110)$ mas, and $\Delta\theta \sim (40, 80)$ mas, respectively. All but the last two events in Table 3 will have $\Delta\theta \gtrsim 110$ mas by 2030, making them accessible down to the hydrogen burning limit at either TMT or EELT, with a few requiring several additional years for access from GMT. KMT-2019-BLG-0371 would only be fully accessible from EELT in 2030.

OGLE-2018-BLG-0677 presents a special case because the 3σ lower limit on its proper motion (derived from Figure 8 of Herrera-Martin et al. 2020) is only 3.7mas yr^{-1} . It is

quite plausible that the Einstein radius of this system is like the others in Table 3, i.e., $\theta_E \sim 115 \mu\text{as}$, in which case $\mu_{\text{rel}} \sim 10 \text{ mas yr}^{-1}$, implying that it would be feasible to image this system in 2030, like the others. This could be tried, but a non-detection would not clearly establish that the host was a BD.

Some progress is possible using present telescopes. For example, MOA-2011-BLG-262 is already separated by $\Delta\theta \sim 130 \text{ mas}$, and so it should be possible to probe companions to a contrast ratio of ~ 5 magnitudes on Keck. However, a non-detection would yield only an upper limit on the host mass that would be well within the stellar range. Note that Bennett et al. (2014) have presented a first epoch for comparison.

If the lens is detected in these observations, then its mass can be reliably inferred from the K -band flux, together with the improved μ_{rel} determination (and so improved $\theta_E = \mu_{\text{rel}} t_E$ determination) from the lens-source separation measurement. Hence, the planet mass can also be determined. Non-detection of the lens would imply that the host is a BD, and would also give an upper limit on the mass of the planet, i.e., $m_p < qM_{\text{H-burn}}$. The relative fraction of BD and stellar hosts would constrain the “mass function”, i.e., the mass function of low-mass stars and BDs that host planets. This could then be compared to the mass function of (apparently) isolated stars and BDs, which can also be obtained from microlensing.

Assuming that future AO observations confirm that the hosts of the planets in Table 3 lie close to the star-BD boundary, such objects host a wide variety of planets. Adopting $M_{\text{host}} = M_{\text{H-burn}} = 0.075 M_{\odot}$ for illustration, the six planets would have (in order of mass) $m_p = [(2, 12, 51, 135, 300)M_{\oplus}, (7.8, 8.8)M_J]$. This distribution already hints at two populations of “planetary” companions of very low mass objects, genuine planets $m_p \lesssim M_J$ formed by core-accretion and much more massive objects $m_p \gg M_J$, drawn from the tail of BDs that are formed by gaseous collapse in a manner similar to stars.

7.2. Patterns of Short-timescale Planetary Events

There are several features of this sample that are important for understanding the detectability of these systems.

One key feature is that in only one of these seven events did followup observations play a role. Indeed, in this case (MOA-2011-BLG-262), follow-up observations (including auto-followup by MOA) were essential in the interpretation of the anomaly. The remaining six cases were survey-only detections, and the KMTNet survey (which began in 2015) was crucial in all six.

Another feature of Table 3 is that the planetary signals for all seven events are generated by resonant or “near-resonant” caustics. Six come from resonant caustics, i.e., the six-sided caustics formed by the “merger” of central and planetary caustics that occurs as $s \rightarrow 1$. One comes from a “near-resonant” caustic structure, which was defined by Yee et al. (2021) as topologically disjoint caustic structures that have ridges (or valleys) of excess magnification of at least 10% that connect the central and planetary caustics. However, this is not surprising. Yee et al. (2021) showed that the great majority of microlensing planets are found in events from these two caustic topologies in roughly the proportion 3:2. Hence, from binomial statistics, the probability that one or fewer from a sample of seven would be near-resonant is $p = 16\%$. Nevertheless, this feature is important in that it means that these systems are detected from relatively short-lived anomalies near the peak of relatively high-magnification events.

Finally, all seven events have faint source-star magnitudes, $I_s > 19.2$. This is mainly explained by the fact that faint sources are much more common than bright ones. However, it does emphasize that in typical real cases, the source has only marginally brightened two days before peak, and has hardly brightened one day before peak. That is, for a typical $t_E \sim 4$ day event on an $I_s = 19.5$ source, the “difference star” on subtracted images is just $I_{\text{diff}} = 19.5$ two days before peak and $I_{\text{diff}} = 18.3$ one day before peak. The OGLE EWS system (Udalski et al. 1994; Udalski 2003) rarely alerts on single-night excursions at this level, and the MOA system (Bond et al. 2001) never does. Moreover, OGLE alerts are usually issued about 10 hours after the end of the night. This explains why there were no such detections based on follow-up observations of OGLE alerts.

By contrast, MOA attempts to issue alerts shortly after a fast-rising event is detected. The MOA threshold of detection is much brighter than OGLE, but for fast-rising events, this is more than compensated by this quick response. In the case of MOA-2011-BLG-262, MOA issued its alert about 6 hr after the first observation of the night, and just 50 min after three observations confirmed a rapid rise. This enabled the first followup observations less than 30 minutes later, allowing full coverage of the anomaly. Without this alert, there would have been only one or two data points over the anomaly. Nevertheless, this is truly a unique example from 14 years of the MOA-II experiment. MOA did not issue alerts for any of the other events in Table 3, except for KMT-2019-BLG-0371, which it alerted at about the mid-point of the anomaly⁷.

⁷Using online MOA and OGLE data that covered only the caustic entrance of KMT-2019-BLG-0371, Valerio Bozza issued an anomaly alert for this event at UT 08:30 on 19 April, which gave a basically correct estimate of the event parameters. However, the anomaly had just ended at the time this alert was issued.

MOA did issue an alert for MOA-2015-BLG-337 on $HJD' = 7214.02$, which would have been plenty of time to initiate intensive observations from Chile at $HJD' \sim 7214.7$, which could have distinguished the two models with q differing by a factor ~ 20 . See Figure 1 from Miyazaki et al. (2018). However, the main team that could have carried out such observations, μ FUN, had discontinued intensive followup observations at this time in order to focus on *Spitzer* microlensing candidates (Yee et al. 2015). There were survey observations from KMTC in Chile, but these commissioning-year data were of insufficient quality. We note that MOA-bin-29 (Kondo et al. 2019) was not discovered in real time, so there was no possibility of followup observations during the 2006 season, and hence there were substantial gaps in the light-curve coverage. Moreover, it is not completely clear that the “Wide-1”/“Wide 3” degeneracy (with different q by a factor 2.7) could have been resolved by additional coverage.

In brief, all six of the survey-only short- t_E planets in Table 3 occurred after the start of KMTNet observations in 2015, and KMTNet data were essential to all six. During the nearly two decades of microlensing planet detections, there has been only one short- t_E planet detected by means of survey-plus-followup observations. The above discussion shows that these patterns are reasonably well understood.

Thus, if the currently very small sample of these important systems is to be increased, the most likely path is to improve the harvest from KMT survey.

7.3. Path to Additional Short- t_E Planetary Events

There are two obvious paths to finding more planetary anomalies in archival short- t_E KMT events. First, as noted by Zang et al. (2021), the online data reductions were substantially improved starting in 2018. Simply applying the same algorithms to 2016 and 2017 data would make it much easier to spot anomalies by eye, or to find them by the automated technique described by Zang et al. (2021). We note that of the six survey-only detections in Table 3, three were from prior to 2018. Of these three, one was not discovered by KMT (OGLE-2015-BLG-1771), one was part of the special 2016 search and so was reduced using the new algorithm (KMT-2016-BLG-2605), and one was a massive planet with a huge, easily discernible anomaly (KMT-2016-BLG-1820). Hence, updating the 2016-2017 reductions, which is currently underway, may well increase the detectability of moderate mass-ratio planets for these seasons⁸.

⁸It is not clear that it will be possible to improve the pipeline light curves for 2015, due to the lower quality of this commissioning-year data. There are currently no plans to do so.

A second path would require a small alteration of the program outlined by Yee et al. (2021) to make TLC reductions for all “high-magnification” events, defined as perhaps $A_{\max} > 20$ or $A_{\max} > 10$. Subtle anomalies, like the one seen in OGLE-2018-BLG-0677 (Herrera-Martin et al. 2020), will only appear convincing (or may only be noticed) in high-quality TLC reductions. Subtle anomalies may reflect very low-mass planets (as in that case), or somewhat higher mass planets in events for which the source passes farther from the caustics. Excluding the two high- q events (KMT-2019-BLG-0371 and KMT-2016-BLG-1820), whose pronounced anomalies are easily recognizable without TLC reductions, the remaining survey-only events have peak magnifications (as judged by $A_{\max} = 1/u_0$) of $A_{\max} = (9, 10, 20, 29)$. And machine PSPL fits could easily underestimate the peak magnification, depending on how these fits were affected by the anomaly. Therefore, the A_{\max} criterion for TLC reductions could be loosened for short- t_E events.

The problems posed by anomaly-dominated events like KMT-2019-BLG-2605 are more challenging. While this event constitutes only 14% of the current sample and may therefore appear relatively inconsequential, it arrived in the sample by a quite accidental route. Hence, it could be under-represented. It would be impractical to repeat the EventFinder searches of archival KMT data, but going forward, the human reviews of the machine-selected EventFinder and AlertFinder (Kim et al. 2018b) candidates could be more aggressive for short events. In particular, when there are magnified data from only one night for each observatory and the event is anomalous, the machine alignment of the data can be radically incorrect, and one or more data sets can even be eliminated from the fit. Recognition of these issues could enable more potentially-anomalous, short events to be conditionally selected at this stage.

For the same reason, it is possible that anomalous EventFinder events that have been selected are being overlooked in manual reviews of the KMTNet webpage. That is, the poor machine alignment of the different data sets can make the event look like “not microlensing”, leading to it not being selected for further analysis. Simple recognition of this possibility, based on the experience of KMT-2016-BLG-2605, may lead to a revised preliminary assessment of such events.

Here, it should be pointed out that archival events are, in some sense, more productive than prospective ones, because they will become eligible for AO imaging sooner.

This research has made use of the KMTNet system operated by the Korea Astronomy and Space Science Institute (KASI) and the data were obtained at three host sites of CTIO in Chile, SAAO in South Africa, and SSO in Australia. Work by C.H. was supported by the grants of National Research Foundation of Korea (2020R1A4A2002885 and

2019R1A2C2085965).

A. Assessment of Source Color

Figure 6 shows OGLE-III (Szymański et al. 2011) stars within a $180''$ circle, centered on the lensing event. The clump is easily visible, but it is extended upper-left to lower-right, which is a standard signature of differential reddening. Hence, we should be cautious about identifying the centroid of the clump feature in this diagram with the center of the clump at the position of the event. Figure 7 shows OGLE-III stars in a $60''$ circle centered on the event. The clump is less visible, but guided by Figure 6, it can be recognized, and its center is marked by a red circle, $[(V - I), I]_{\text{cl}} = (3.42, 16.98) \pm (0.02, 0.04)$. This same position is marked by a circle in Figure 6, which demonstrates that the centroid of the clump feature has indeed shifted fainter and redder from the first to the second figure.

The source magnitude is well measured from the microlensing fit in the KMTS pyDIA system, $I_{s,\text{kmts}} = 20.06 \pm 0.04$. By comparing field-star photometry from OGLE-III with that of the KMTS pyDIA reductions, we find $I_{\text{kmts}} - I_{\text{ogle-iii}} = -0.15 \pm 0.01$, implying $I_{s,\text{ogle-iii}} = 20.21 \pm 0.05$. Hence, the offset in brightness of the source relative to the clump is

$$\Delta I = I_s - I_{\text{cl}} = 3.23 \pm 0.07. \quad (\text{A1})$$

However, the color offset $\Delta(V - I)$ is substantially more difficult to determine. There is only one substantially magnified V -band data point. This would make it difficult to measure the source color under any circumstances because there would be no internal check on the measurement. In addition, as we report below, the image quality of the one magnified V -band point exhibits some problems. We therefore begin by asking what can be deduced about the source color without a measurement from the light curve.

Figure 8 shows the *Hubble Space Telescope (HST)* CMD for a Baade Window field constructed by Holtzman et al. (1998). The red circle shows the clump centroid $[(V - I), I]_{\text{BW}} = (1.62, 15.15)$ as determined by Bennett et al. (2008). The two magenta lines are displaced ± 0.1 (i.e., 1.5σ) from the best estimate of the offset (Equation (A1)) for KMT-2016-BLG-2605, $\Delta I = 3.23$. Based on the stars between these two lines, we can make three different characterizations of the stars at this offset:

$$-0.47 < \Delta(V - I) < -0.01; \quad \langle \Delta(V - I) \rangle = -0.31 \pm 0.09; \quad \Delta(V - I)_{\text{median}} = -0.32_{-0.07}^{+0.08}. \quad (\text{A2})$$

The first is the full “reasonably populated” region of the strip. The second is the mean and standard deviation of this populated region. The third is the median and (16,84)th

percentiles of the full distribution. If there were absolutely no other information about the source color, one would take either the mean or median estimator, which in the present case are almost identical.

We will next consider the color measurement based on the light curve, i.e., on the single magnified V -band measurement. However, before proceeding, we should “predict” the KMTS V -band flux measurement at $\text{HJD}' = 7565.4446$ based on the contemporaneous I -band flux measurement ($F_I = 35688 \pm 325$), and the range of “reasonably populated” $\Delta(V - I)$ given by Equation (A2). To do so, we take note of the offset (measured from field stars) $(V - I)_{\text{kmts}} - (V - I)_{\text{ogle-iii}} = 0.27 \pm 0.02$, the KMTS instrumental photometric zero points ($V_{\text{zero}} = 28.65$ and $I_{\text{zero}} = 28.00$), and the OGLE-III clump centroid $(V - I)_{\text{cl}} = 3.42 \pm 0.02$. That is,

$$F_{V,\text{predicted}} = 0.0608 F_I \times 10^{-0.4\Delta(V-I)} \rightarrow 2170 \times 10^{-0.4\Delta(V-I)}, \quad (\text{A3})$$

and hence, for the full “reasonable range” of $\Delta(V - I)$, we predict, $2200 < F_{V,\text{predicted}} < 3360$, which should be compared to the observed V -band difference flux returned by the photometry program, $F_V = 1545 \pm 238$. That is, the observed flux lies 2.75σ below the “reasonable range”. This could mean that the source is a very rare, exceptionally red star, that the error bar has been substantially underestimated, or that the measured value is the outcome of a rare statistical fluctuation.

We find no evidence that the photometry program has generally underestimated the error bars on the V -band light-curve measurements. In particular, we look at the distribution of σ_i/F_i of the 87 measurements apart from the well-magnified one and the one on the previous night at modest magnification (for which the predicted difference flux is $< 1\sigma$). For these 87, the expected difference flux is zero to high precision. We find that this distribution is consistent with a Gaussian of zero mean and unit variance.

We examine the original and subtracted images for the magnified point and compare these to several images for unmagnified points. In the original images, the source generally appears isolated, and there are only very faint stars within a few arcseconds. With the exception of the magnified point, the subtracted images generally appear “blank” at, and for several arcseconds around, the source. Hence, there is no obvious cause for difficulty in performing the photometry, in line with the fact (just reported) that the normalized error distribution is a unit Gaussian.

The magnified image is taken seven days after passage of the full moon through the bulge, so that the background is about 2.8 times the dark-time level. As a result of this higher background, the subtracted image appears substantially more mottled than for dark-time images. Nevertheless, the background level (453 ADU per pixel) is by no means high.

Similarly, the seeing has a $\text{FWHM}_{\text{see}} \sim 2.75''$, which is higher than the median ($2.39''$), but hardly unusual (66th percentile). And also similarly, the transparency is about 88% relative to typical good nights, which is hardly out of the normal range.

Finally, we consider the general possibility that the program has underestimated the error bar for some “unknown reason”. The program makes its estimate by varying the fit parameters and finding the change of χ^2 that results. This should be robust, but for any relatively complex program, one can imagine that it confronts some unexpected condition and makes a catastrophic error. As a sanity check, we make a naive estimate of the error as being proportional to $[\text{FWHM}_{\text{see}} \times (\text{FWHM}_{\text{back}}/\text{transparency})^{1/2}]$, where $\text{FWHM}_{\text{back}}$ is the full width at half maximum of the difference-flux pixel-count distribution of the subtracted image. For images that are well below sky, this scaling should be close to accurate. We normalize this estimator to an image with low background (164), good seeing ($1.51''$) and 100% relative transparency and find only a 19% difference in predicted versus reported error bars. This is an order of magnitude below what would be required to explain the apparent discrepancy (and also goes in the wrong direction).

In brief, the source location is isolated, the program overall evaluates the V -band errors correctly, the seeing and background of the magnified image are slightly worse than average but by no means unusual, and a simple sanity check confirms the program’s evaluation of the error bar.

If the 2.75σ discrepancy between prior expectations and the observed data point are to be explained within the context of Gaussian statistics, then $p_{\text{gauss}} = 0.0031$. Therefore, before accepting this explanation, we should consider various others that are of such low probability that they would normally be dismissed without detailed investigation.

First, the source may actually be drawn from the extremely red population that is the reflected in the *HST* CMD. Of the 414 stars shown between the magenta lines, two are within the 1σ range of the magnified point, $\Delta(V - I) = +0.37 \pm 0.17$, and one other is redward of this range. This fraction, $3/414 = 0.007$, is greater than p_{gauss} , and so this possibility should be considered. However, from the morphology of Figure 8, these very red stars appear to be part of the disk red-dwarf population that lives “above” the bulge main sequence in this diagram. As such, the red stars within the magenta bands lie about 3 mag in front of the bulge in distance modulus, i.e., at about $D_S = 2$ kpc. In addition to being extremely rare (as just noted), the optical depth to microlensing of such nearby disk sources is two orders of magnitude lower than for bulge sources. Thus, we regard this potential explanation as highly improbable.

Bensby et al. (2017) provide some corroboration of this assessment. They obtained 91

high-resolution spectra of highly-magnified “dwarf and subgiant” sources. These were almost all selected solely on source-brightness relative to the clump (i.e., not giants) and observability (magnified enough to obtain a good spectrum), which in practice essentially produced an unbiased sample of turnoff stars and subgiants. None of these 91 had spectroscopic temperatures cooler than the clump (~ 4750 K). See upper panel of their Figure 7. While 0/91 does not place restrictions at the level of p_{gauss} , it does demonstrate that such extremely red microlensed sources lying 3 mag below the clump are very rare.

Another possibility is that the microlensing model is incorrect, so that the source is actually brighter (relative to the clump) than the magenta band. For example, the source is 0.8 mag brighter for Local 3 than for Local 1. However, the *HST* CMD is even less populated 0.8 mag above the red end of the magenta band than in the band itself. One might posit that there is another solution with an even brighter source that we failed to discover. However, the source cannot be much brighter⁹ than the baseline object, which is only $-2.5 \log(1 + f_B/f_S) = -1.5$ mag brighter than the magenta bar. This is still far below the region of the CMD that is populated by upper giant-branch stars.

Yet another possibility is that the source is actually a giant in the far side of the disk. There would be extremely few such stars in the *HST* CMD because it lies in the Baade Window at $b \sim -4$, so that the line of sight intersects the bulge about $z_{\text{bulge}} \sim -550$ pc from the Galactic plane. Far-disk sources are more plausible for KMT-2016-BLG-2605 for which $b = -1.6$, so that $z_{\text{bulge}} \sim -210$ pc. For example, at $D_S = 12$ kpc, the line of sight passes $z_{12 \text{ kpc}} \sim -320$ pc from the plane, where potential source stars remain plentiful. Nevertheless, in order to access the red upper-giant-branch stars, the source would have to have a distance modulus at least 2.5 larger than the bulge, i.e., $D_S > 25$ kpc or $\sim 2R_0$ from the Galactic center on the far side of the Galaxy, with $z_{25 \text{ kpc}} \sim -700$ pc from the plane. This is a very thinly populated region of the Galaxy. While we do not exclude this possibility, and we report its implications further below, we consider it less likely than a statistical error in the *V*-band measurement.

We conclude that the most plausible resolution is that the source color is toward the red end of the “reasonable range” from Equation (A2) and that the very red light-curve measurement is the result of a relatively large statistical fluctuation. We therefore adopt

$$\Delta(V - I)_s = -0.06 \pm 0.05 \Rightarrow (V - I)_{s,0} = 1.00 \pm 0.05 \quad (\text{A4})$$

However, we also consider the possibility that the light-curve measurement is actually correct

⁹It could be slightly brighter because the source might be projected against a “hole” in the mottled background due to unresolved field stars (Park et al. 2004). However, this effect is far too small to be relevant here.

(due, e.g., to a very distant far-disk source), i.e., $(V - I)_0 = 1.43 \pm 0.17$, and thus we trace the consequences of this possibility.

A.1. Effects of Alternate Color Estimate

We have adopted a source color $(V - I)_s = 3.37 \pm 0.05$ (equivalently, $(V - I)_{s,0} = 1.00 \pm 0.05$) by combining prior information from the Holtzman et al. (1998) CMD with the KMTS color measurement. Here, we consider the consequences if the source color is actually given by the KMTS measurement, i.e., $(V - I)_s = 3.89 \pm 0.17$ (equivalently, $(V - I)_{s,0} = 1.43 \pm 0.17$).

The first point is that the true source color can eventually be determined by high-resolution imaging, and indeed this may already be possible with 10m-telescope class AO imaging. Using Bessell & Brett (1988) to convert from $(V - I)$ to $(I - K)$, and adopting $E(I - K) = 2.35$ from Section 2, we find $K_s = 16.48 \pm 0.08$ or $K_s = 15.96^{+0.35}_{-0.19}$, for the two scenarios. These values can be compared to the K -band magnitude of the baseline object from the VVV survey (Minniti et al. 2017) of $K_{\text{base}} = 14.89 \pm 0.07$. That is, roughly 23% or 37% of the baseline-object K -band light comes from the source.

There are logically only four possibilities for the remainder of the K -band light: the lens, a companion to the lens, a companion to the source, or an ambient star (or some combination). It is very unlikely that an ambient star would lie within the ~ 55 mas point-spread function (PSF) of a 10m telescope. If the blended light were due to the lens or a companion to the lens, then by 2021, it would have already separated from the source by $\Delta\theta = \mu_{\text{rel}}\Delta t = 61 \pm 5$ mas (or 79 ± 7 mas). In either case, the source and lens could be separately resolved. See Figure 1 of Bennett et al. (2020) for a separate resolution of a source and lens with flux ratio 3.15 at $\Delta\theta = 55$ mas, and Figure 1 of Bhattacharya et al. (2019) for an unambiguous distinction between a source and lens with flux ratio 1.46 at $\Delta\theta = 34$ mas, both based on K -band observations with the Keck telescope. Thus, unless the blended light is due to a companion to the source (which would then be a lower-giant-branch star, which is a priori unlikely due to its short lifetime), the source color could almost certainly be determined by observations in 2021.

Such immediate observations might also resolve the lens, and, even if not, would give a definite prediction as to when the lens could be resolved. For example, suppose that these observations found that $K_s = 15.96$ (with small error). One could then conclude that $\mu_{\text{rel}} = 15.8 \pm 0.8$ mas yr $^{-1}$ so that the annulus of possible lens positions (at 1.5 FWHM) could be predicted with precision. Hence, one could already detect the lens, or place strong constraints on its brightness. If the source proved to be substantially fainter in K , this

would imply a smaller θ_E and hence a smaller μ_{rel} . However, it would still be possible to use this information to predict when the lens would be observable. As discussed in Section 7.1 non-detection of the lens in relatively shallow imaging would indicate the need for deeper imaging, either on 10m or future 30m class telescopes.

REFERENCES

- Alard, C. & Lupton, R.H., 1998, *ApJ*, 503, 325
- Albrow, M.D. Michaelalbrow/Pydia: InitialRelease On Github., vv1.0.0, Zenodo
- Albrow, M. D., Horne, K., Bramich, D. M., et al. 2009, *MNRAS*, 397, 2099
- Batista, V., Gould, A., Dieters, S. et al. *A&A*, 529, 102
- Bennett, D.P., Bond, I.A., Udalski et al. 2008, *ApJ*, 684, 663
- Bennett, D.P., Sumi, T., Bond, I.A., et al. 2012, *ApJ*, 757, 119
- Bennett, D.P., Batista, V., Bond, I.A., et al. 2014, *ApJ*, 785, 155
- Bennett, D.P., Bhattacharya, A., Beaulieu, J.-P., et al. 2020, *AJ*, 159, 68
- Bensby, T. Yee, J.C., Feltzing, S. et al. 2013, *A&A*, 549, A147
- Bensby, T. Feltzing, S. Gould, A., et al. 2017, *A&A*, 605, A89
- Bessell, M.S., & Brett, J.M. 1988, *PASP*, 100, 1134
- Bhattacharya, A., Beaulieu, J.-P., Bennett, D.P., et al. 2019, *AJ*, 156, 289
- Bond, I.A., Abe, F., Dodd, R.J., et al. 2001, *MNRAS*, 327, 868
- Bowler, B.P, Liu, M.C., Shkolnik, E.L., Tamura, M. 2015, *ApJS*, 216, 7
- Gould, A. 1996, *ApJ*, 470, 201
- Gould, A. & Loeb, A. 1992, *ApJ*, 396, 104
- Gould, A., Dong, S., Bennett, D.P. et al. 2010, *ApJ*, 710, 1800
- Gould, A., Zang, W., Mao, S., & Dong, S., 2021a, *RAA*, in press, arXiv:2010.00957
- Griest, K. & Safizadeh, N. 1998, *ApJ*, 500, 37

- Groenewegen, M.A.T., 2004, MNRAS, 353, 903
- Han, C., Shin, I.-G., Jung, Y. K., et al. 2020, A&A, 641A, 105
- Herrera-Martin, A., Albrow, A., Udalski, A., et al. 2020, AJ, 159, 134
- Holtzman, J.A., Watson, A.M., Baum, W.A., et al. 1998, AJ, 115, 1946
- Hwang, K.-H., Udalski, A., Bond, I.A., et al. 2018, AJ, 155, 259
- Jung, Y. K., Gould, A., Udalski, A., et al. 2018a, AJ, 155, 219
- Jung, Y. K., Hwang, K.-H., Ryu, Y.-H., et al. 2018b, AJ, 156, 208
- Jung, Y. K., Han, C., Udalski, A., et al. 2021, AAS submitted, arXiv:2102.07338
- Kervella, P., Thévenin, F., Di Folco, E., & Ségransan, D. 2004, A&A, 426, 297
- Kim, S.-L., Lee, C.-U., Park, B.-G., et al. 2016, JKAS, 49, 37
- Kim, D.-J., Kim, H.-W., Hwang, K.-H., et al., 2018a, AJ, 155, 76
- Kim, D.-J., Hwang, K.-H., Shvartzvald, et al. 2018b, arXiv:1806.07545
- Kim, H.-W., Hwang, K.-H., Gould, A., et al. 2020, AAS submitted, arXiv:2007.06870
- Kim, Y.H., Chung, S.-J., Yee, J.-C., et al. 2021, AAS submitted, arXiv:2101.12206
- Kondo, I., Sumi, T., Bennett, D.P., et al. 2019, AJ, 258, 224
- Mao, S. & Paczyński, B. 1991, ApJ, 374, 37
- Miyazaki, S., Sumi, T., Bennett, D.P., et al. 2018, AJ, 156, 136
- Minniti, D., Lucas, P., VVV Team, 2017, yCAT 2348, 0
- Mróz, P., Poleski, R., Gould, A., et al. 2020, ApJ, 903, 11
- Nataf, D.M., Gould, A., Fouqué, P. et al. 2013, ApJ, 769, 88
- Paczynski, B. 1986, ApJ, 304, 1
- Park, B.-G., DePoy, D.L., Gaudi, B.S., et al. 2004, ApJ, 609, 166
- Ryu, Y.-H., Mroz, P., Gould, A. et al. 2021, AJ, 161, 126
- Szymański, M.K., Udalski, A., Soszyński, I., et al. 2011, Acta Astron., 61, 83

Tomaney, A.B. & Crotts, A.P.S. 1996, AU, 112, 2872

Udalski, A. 2003, Acta Astron., 53, 291

Udalski, A., Szymanski, M., Kaluzny, J., Kubiak, M., Mateo, M., Krzeminski, W., & Paczyński, B. 1994, Acta Astron., 44, 227

Yee, J.C., Shvartzvald, Y., Gal-Yam, A. et al. 2012, ApJ, 755, 102

Yee, J.C., Gould, A., Beichman, C., 2015, ApJ, 810, 155

Yee, J.C., Zang, W., Udalski, A. et al. 2021, AAS submitted, arXiv:2101.04696

Yoo, J., DePoy, D.L., Gal-Yam, A. et al. 2004, ApJ, 603, 139

Zang, W., , Hwang, K.-H., Udalski, A., et al. 2021, in prep

Zhang, X., Zang, W., Udalski, A., et al. 2020, AJ, 159, 116

Table 1. BEST SOLUTIONS WITHOUT FLUX CONSTRAINT

Parameters	Local 1	Local 1a	Local 1b	Local 2	Local 3
χ^2/dof	3596.308/3598	3603.450/3598	3605.222/3598	3606.825/3598	3606.218/3598
$t_0 - 2457560$	5.451 ± 0.021	5.457 ± 0.010	5.473 ± 0.010	5.643 ± 0.023	5.473 ± 0.013
u_0	0.049 ± 0.004	0.046 ± 0.004	0.047 ± 0.004	0.097 ± 0.006	0.085 ± 0.007
t_E (days)	3.370 ± 0.139	3.291 ± 0.123	3.023 ± 0.146	2.237 ± 0.057	2.319 ± 0.104
s	0.939 ± 0.011	0.924 ± 0.006	0.914 ± 0.004	1.827 ± 0.064	0.797 ± 0.014
q	0.012 ± 0.002	0.013 ± 0.002	0.007 ± 0.001	0.242 ± 0.074	0.019 ± 0.003
α (rad)	0.101 ± 0.019	0.180 ± 0.018	0.057 ± 0.031	2.580 ± 0.040	-0.042 ± 0.065
ρ (10^{-2})	1.203 ± 0.125	1.068 ± 0.079	1.145 ± 0.156	3.345 ± 0.262	1.651 ± 0.269
f_S [KMTC]	0.151 ± 0.016	0.163 ± 0.011	0.206 ± 0.024	0.320 ± 0.023	0.336 ± 0.032
f_B [KMTC]	0.388 ± 0.016	0.376 ± 0.011	0.332 ± 0.024	0.220 ± 0.023	0.203 ± 0.032
f_S [KMTS]	0.151 ± 0.010	0.141 ± 0.009	0.170 ± 0.014	0.389 ± 0.023	0.314 ± 0.026
f_B [KMTS]	0.436 ± 0.010	0.446 ± 0.009	0.417 ± 0.014	0.198 ± 0.023	0.273 ± 0.026
f_S [KMTA]	0.096 ± 0.006	0.090 ± 0.005	0.103 ± 0.009	0.234 ± 0.013	0.200 ± 0.016
f_B [KMTA]	0.270 ± 0.006	0.276 ± 0.005	0.263 ± 0.009	0.133 ± 0.013	0.167 ± 0.016
$I_{S,\text{kmts}} - I_{S,\text{kmtc}}$	-0.002 ± 0.066	0.152 ± 0.062	0.208 ± 0.048	-0.213 ± 0.049	0.072 ± 0.045
t_* (days)	0.041 ± 0.004	0.035 ± 0.002	0.035 ± 0.003	0.075 ± 0.005	0.038 ± 0.005

Table 2. BEST SOLUTIONS WITH FLUX CONSTRAINT

Parameters	Local 1	Local 2	Local 3
χ^2/dof	3597.963/3599	3622.808/3599	3613.757/3599
$t_0 - 2457560$	5.451 ± 0.005	5.553 ± 0.039	5.500 ± 0.008
u_0	0.049 ± 0.004	0.091 ± 0.012	0.081 ± 0.007
t_E (days)	3.405 ± 0.128	2.207 ± 0.071	2.402 ± 0.100
s	0.940 ± 0.005	1.756 ± 0.093	0.787 ± 0.008
q	0.012 ± 0.001	0.175 ± 0.092	0.023 ± 0.002
α (rad)	0.104 ± 0.010	2.483 ± 0.097	0.053 ± 0.043
ρ (10^{-2})	1.192 ± 0.083	3.683 ± 0.283	1.298 ± 0.203
f_S [KMTC]	0.145 ± 0.009	0.354 ± 0.031	0.291 ± 0.025
f_B [KMTC]	0.393 ± 0.009	0.186 ± 0.031	0.248 ± 0.025
f_S [KMTS]	0.150 ± 0.009	0.364 ± 0.032	0.300 ± 0.025
f_B [KMTS]	0.437 ± 0.009	0.223 ± 0.032	0.287 ± 0.025
f_S [KMTA]	0.095 ± 0.006	0.223 ± 0.018	0.190 ± 0.016
f_B [KMTA]	0.271 ± 0.006	0.144 ± 0.018	0.176 ± 0.016
$I_{S,\text{kmts}} - I_{S,\text{kmtc}}$	-0.033 ± 0.005	-0.032 ± 0.005	-0.033 ± 0.005
t_* (days)	0.041 ± 0.002	0.081 ± 0.005	0.031 ± 0.004

Table 3. 7 PLANETARY EVENTS WITH $t_E < 7$ DAYS

Event	t_E	q	$\ln s$	θ_*	θ_E	μ_{rel}	I_s	Caustic Type
KMT-2016-BLG-2605	3.41	0.0120	-0.06	1.38	116	12.3	20.21	Resonant
MOA-2011-BLG-262	3.87	0.00047	± 0.05	0.78	136	12.9	19.34	Resonant
OGLE-2015-BLG-1771	4.28	0.00538	0, +0.18	0.49	111	9.5	21.77	Resonant
KMT-2018-BLG-0748	4.38	0.00203	-0.06	1.21	111	9.2	19.21	Resonant
KMT-2016-BLG-1820	4.81	0.11300	+0.15	0.81	123	9.3	19.38	Resonant
OGLE-2018-BLG-0677	4.94	0.00008	-0.09, -0.02	0.79	> 49	> 3.6	19.32	Near-Resonant
KMT-2019-BLG-0371	6.53	0.08, 0.12	-0.19, +0.45	0.92	135	7.6	19.76	Resonant

Note. — t_E is in days, θ_* and θ_E are in μas , and μ_{rel} is in mas yr^{-1} .

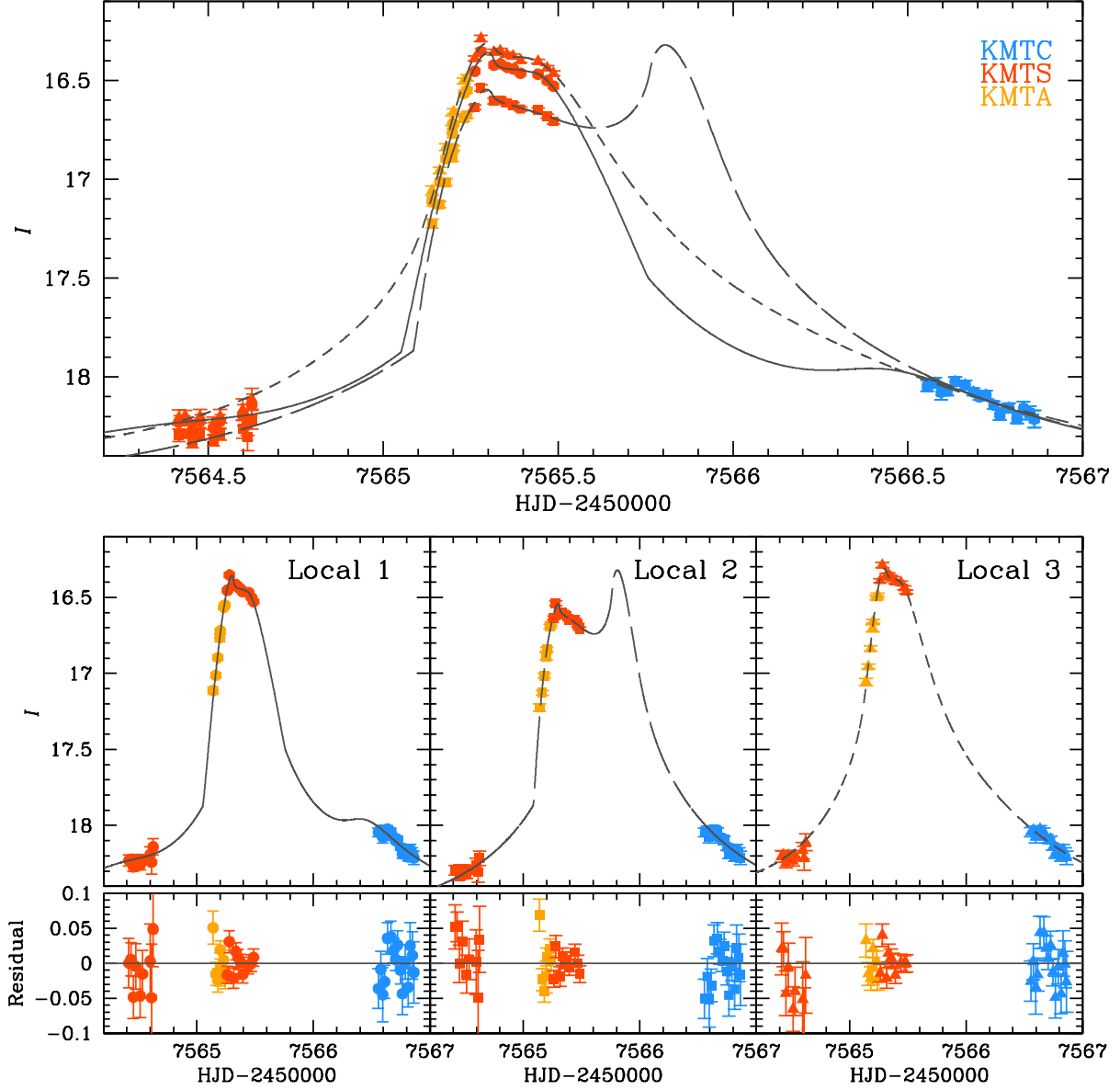


Fig. 1.— Light curve and models for Locals 1–3 for KMT-2016-BLG-2605. Upper Panel: In contrast to the great majority of microlensing events, the data points for competing models are offset from one another for both of the non-anchor observatories (KMTS and KMTA). By construction, they are perfectly aligned for the anchor (flux-reference) observatory (KMTC). These offsets occur because each observatory has only one night of strongly magnified data. See Section 2. The middle and bottom rows of panels show the individual models and their residuals, respectively. By eye, Local 1 better matches the data. Formally, the fit is better by $\Delta\chi^2 \gtrsim 10$. See Table 1.

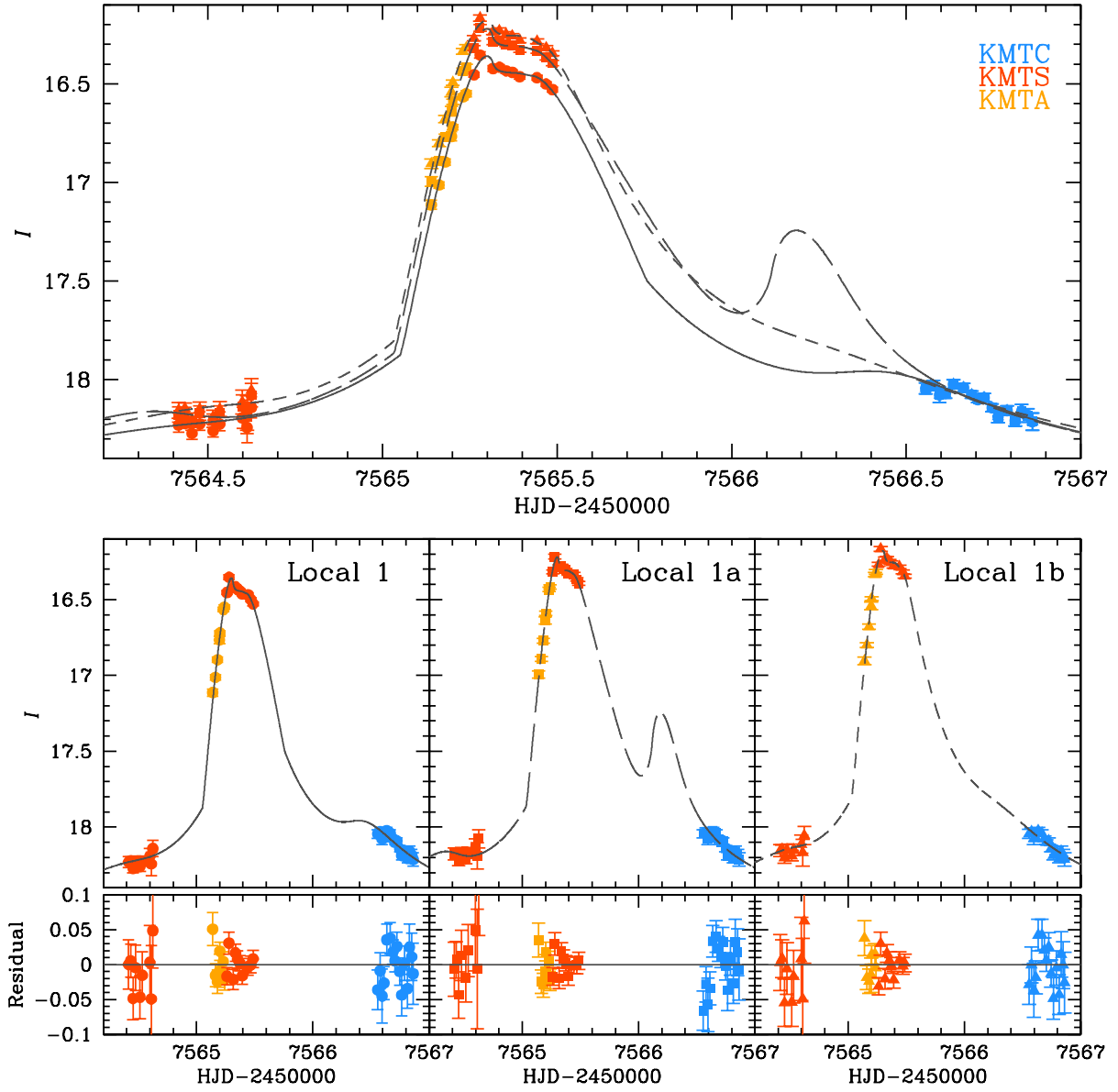


Fig. 2.— Similar to Figure 1, but for Local 1 and its two satellite solutions, Local 1a, and Local 1b. By eye, Local 1 is favored over the other two, but less decisively than for Figure 1. See Table 1.

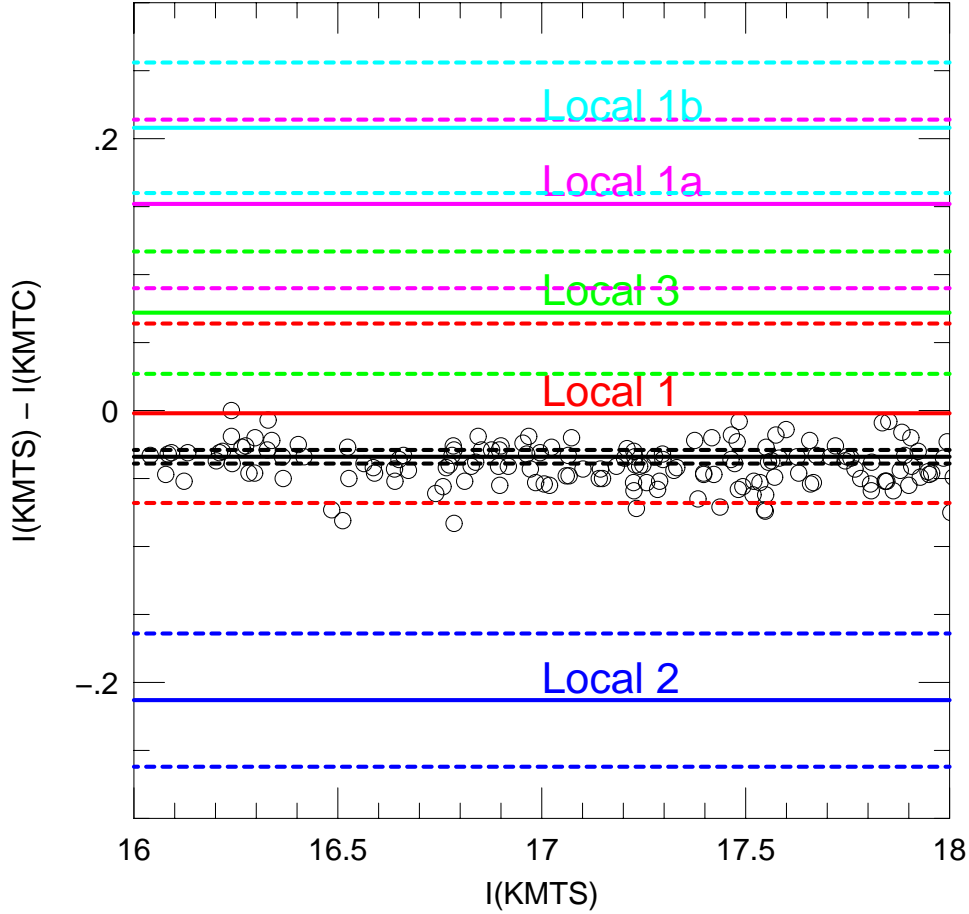


Fig. 3.— Offset between KMTS and KMTC I -band photometry as determined from field stars (open circles), compared to the predictions of the five different models shown in Figures 1 and 2. See the penultimate row of Table 1. There is 1σ agreement for Local 1 and $\geq .3\sigma$ disagreement for all the others. After incorporating the flux constraint (black dashed band) into the MCMC, Locals 1a and 1b are eliminated as distinct minima, while Locals 2 and 3 become disfavored by $\Delta\chi^2 \gtrsim 16$. See Table 2.

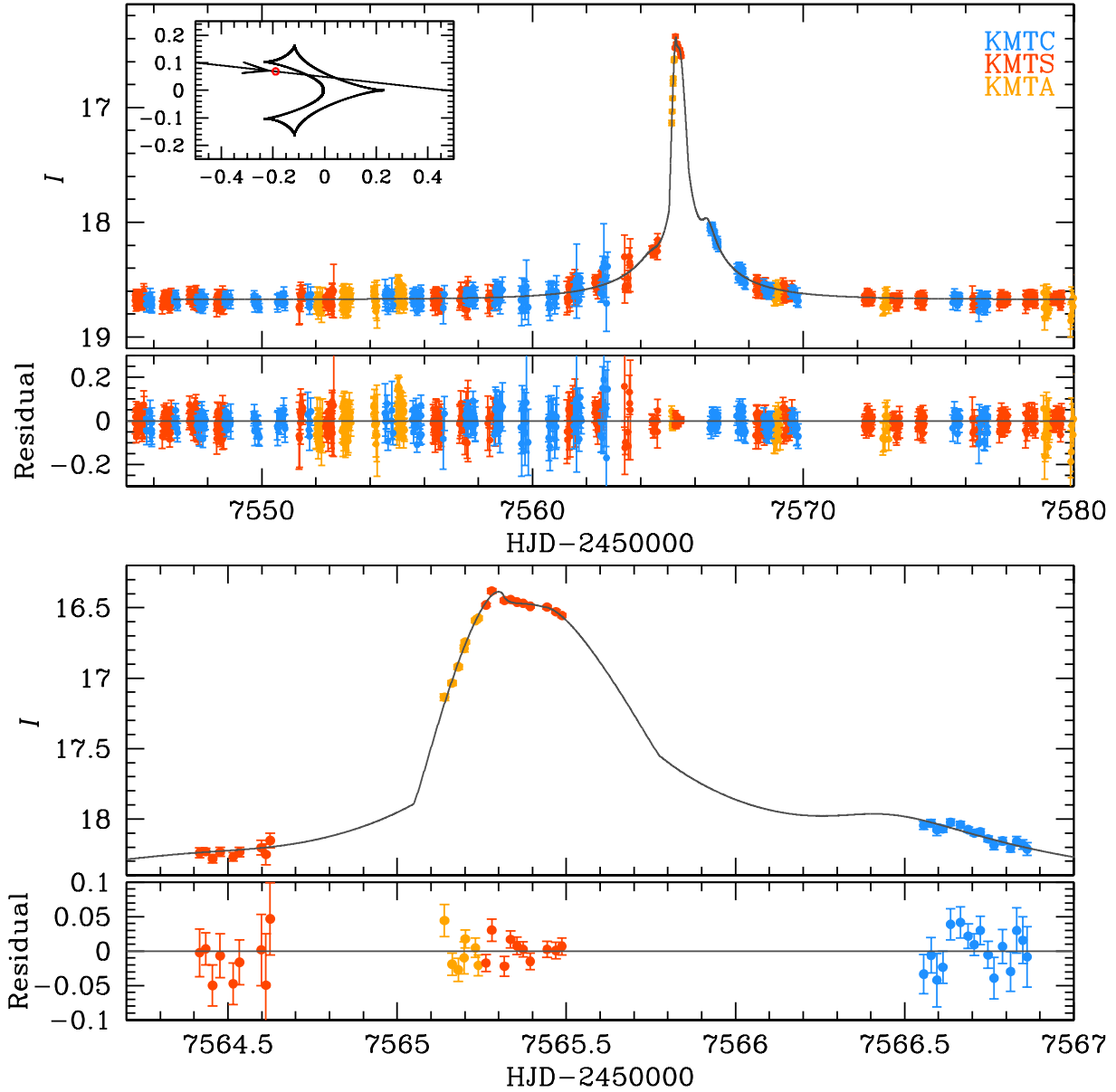


Fig. 4.— Light curve and models for Local 1 for KMT-2016-BLG-2605, after incorporating the flux constraint shown in Figure 3. Also shown is the caustic topology for the event.

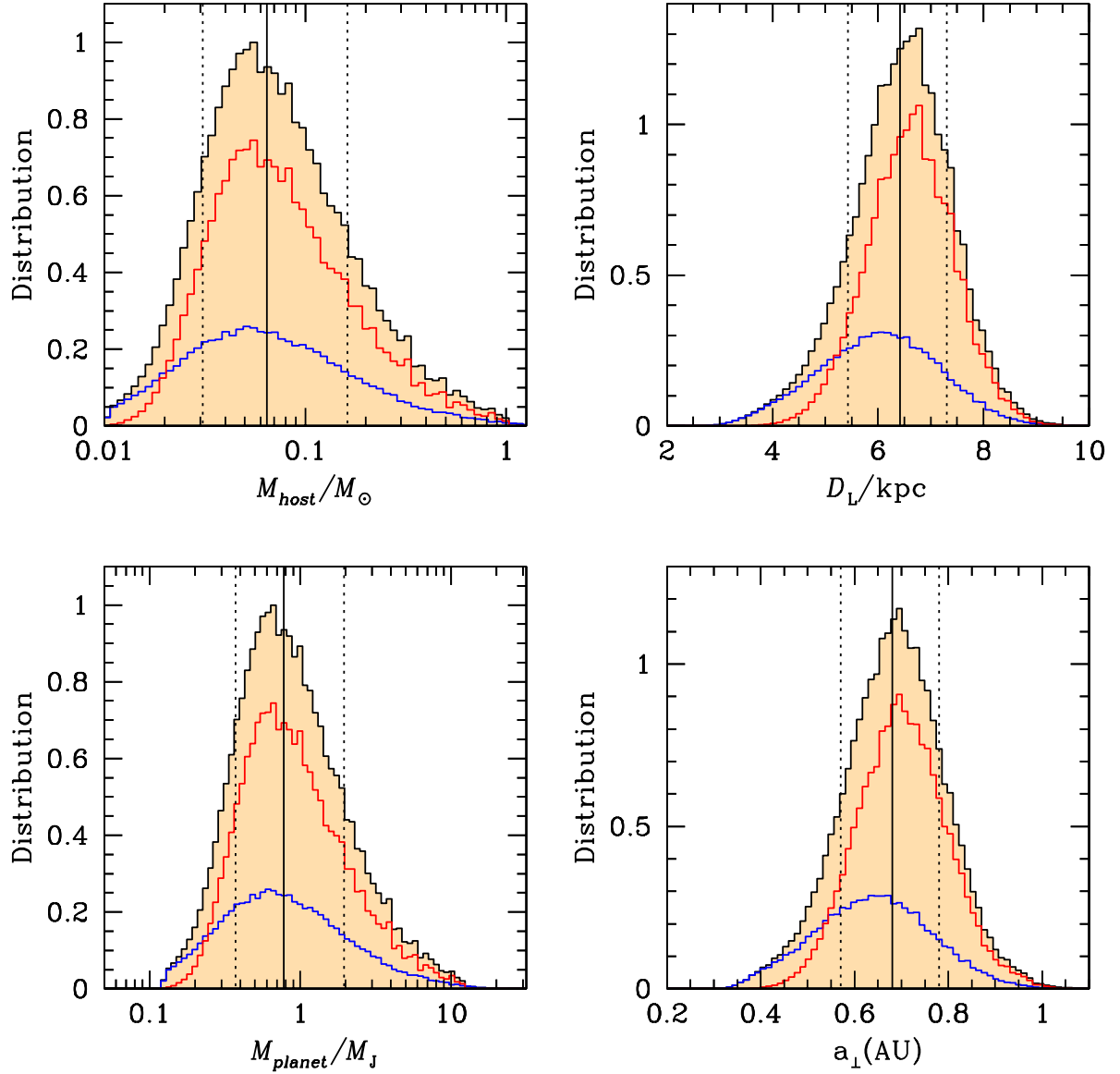


Fig. 5.— Bayesian estimates of the host mass, planet mass, system distance, and planet-host projected separation for KMT-2016-BLG-2605. The red and blue histograms show the relative contributions of bulge and disk lenses, respectively, with the total are shown as black histograms. The median host mass is very close to the star-BD boundary.

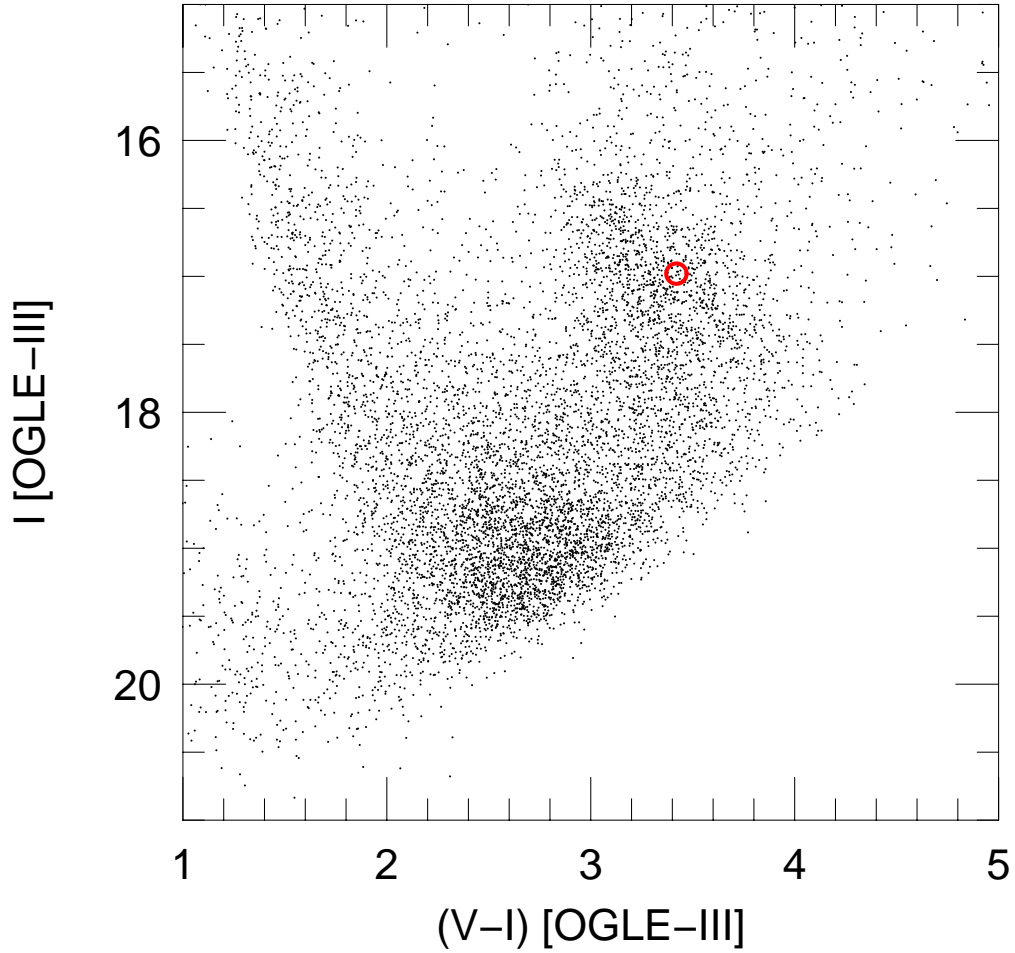


Fig. 6.— OGLE-III (Szymański et al. 2011) CMD for stars within $180''$ of KMT-2016-BLG-2605. The clump is clearly visible, but is extended from upper left to lower right, indicating strong differential reddening. The red circle is the clump center as determined from the $60''$ CMD in Figure 7, which is clearly not aligned with the center of the clump “feature” in this diagram.

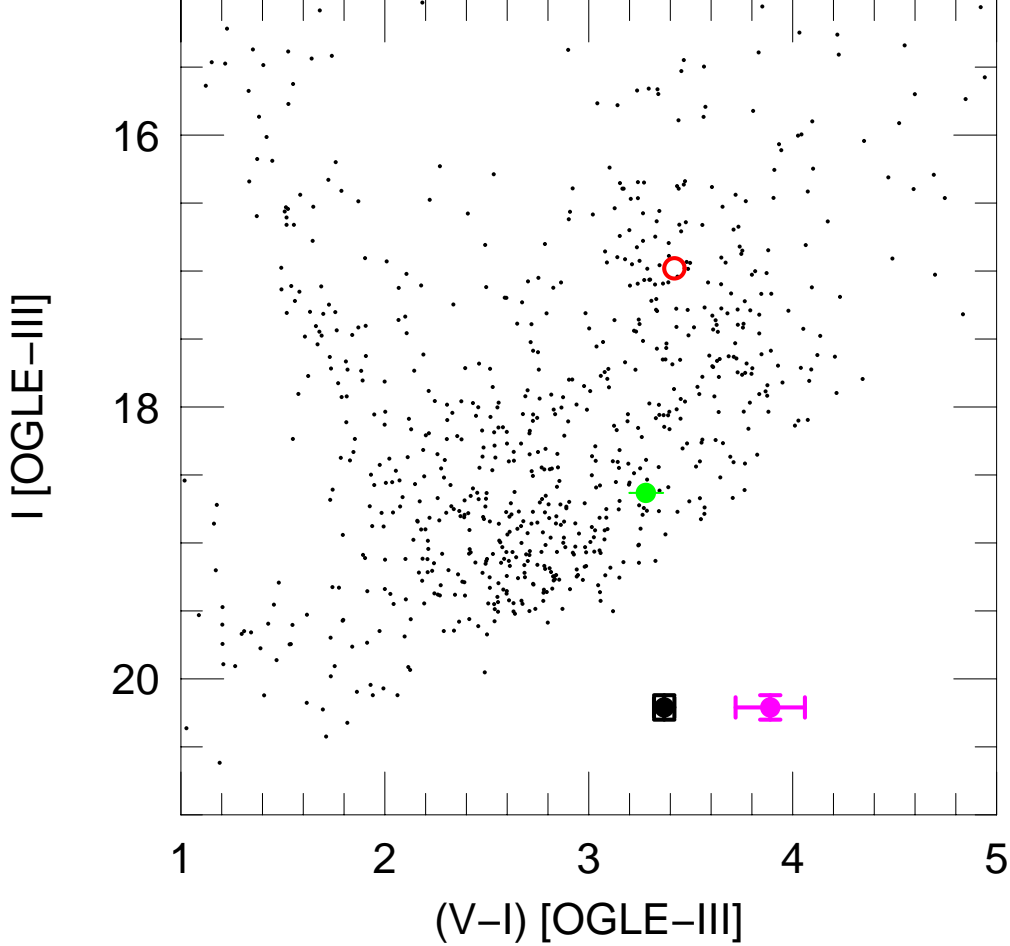


Fig. 7.— OGLE-III CMD for stars within $60''$ of KMT-2016-BLG-2605. The clump is less clearly visible than in Figure 6 but with the aid of that figure it can be identified. The red circle is the clump centroid. The magenta circle represents the CMD position of the source as determined from the light curve alone. The black circle is the adopted CMD source position after incorporating information from the *HST* CMD shown in Figure 8. The implications of these two different source positions and how they can eventually be distinguished is discussed in the Appendix. The green circle represents the baseline-object position $[(V - I), I]_{\text{base}}$, where $I_{\text{base}} = 18.63$ comes directly from the OGLE-III catalog (Szymański et al. 2011) and $(V - I)_{\text{base}} = 3.28$ is derived by combining I_{base} with $K_{\text{base}} = 14.89 \pm 0.07$ from the VVV catalog (Minniti et al. 2017), and then transforming from $(I - K)$ to $(V - I)$ using matched stars between OGLE-III and VVV. The K magnitude of the baseline object can be helpful in future AO imaging. See the Appendix.

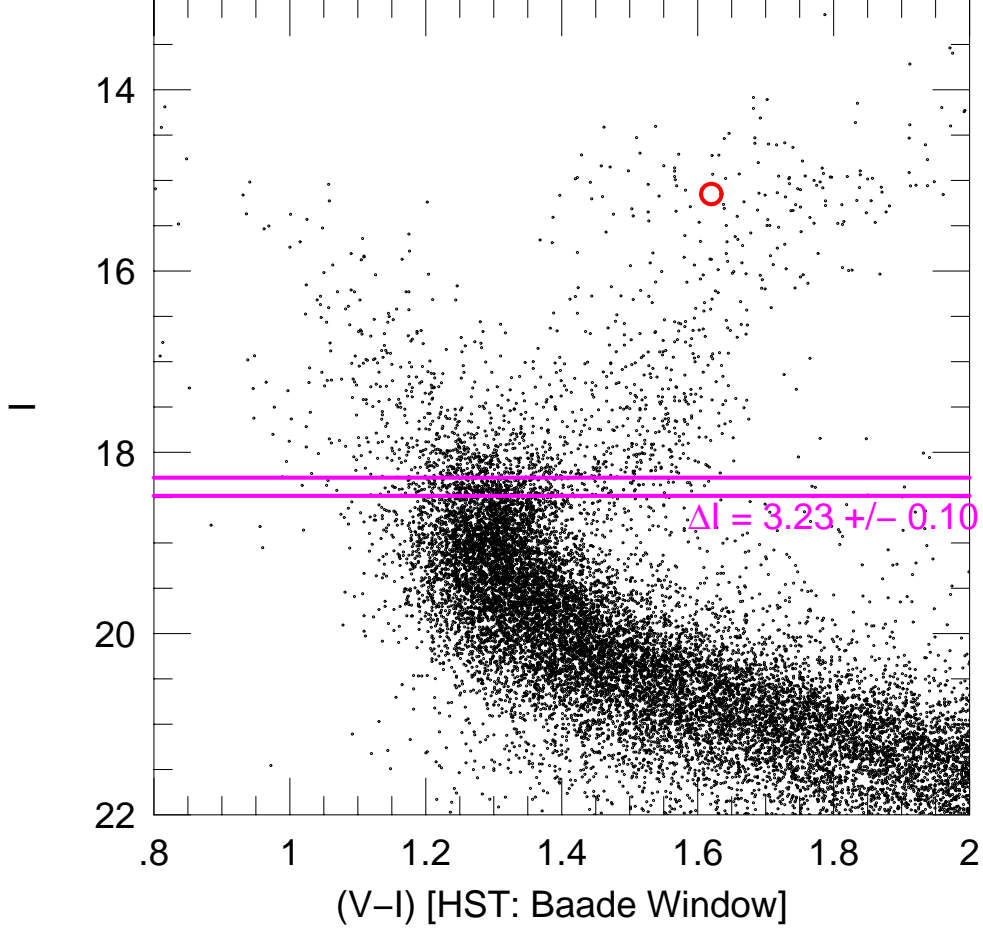


Fig. 8.— *HST* CMD from the observations of the Baade Window by (Holtzman et al. 1998). The clump centroid, marked by a red circle, is at $[(V - I), I]_{\text{cl}} = (1.62, 15.15)$ (Bennett et al. 2008). The magenta lines, lying $\Delta I = 3.23 \pm 0.10$ below the clump represent the 1.5σ range for the source brightness relative to the clump. The source color, based on a single KMTS *V*-band measurement is $\Delta(V - I) = 0.37 \pm 0.17$ redward of the clump. So, on this diagram it would be at $(V - I)_{\text{HST,BW}} = 1.99 \pm 0.17$, i.e., at the extreme right of the magenta band. However, it is not shown to avoid clutter. See the Appendix for why this is most likely due to a large statistical fluctuation. The adopted color offset is $\Delta(V - I)_s = -0.06 \pm 0.05$, consistent with the subgiants at $(V - I)_{\text{HST,BW}} = 1.56 \pm 0.05$ in this diagram. See black circle in Figure 7

Table 4. PHYSICAL PARAMETERS

Quantity	Local 1
$M_{\text{host}} [M_{\odot}]$	$0.064^{+0.099}_{-0.033}$
$M_{\text{planet}} [M_J]$	$0.771^{+1.183}_{-0.401}$
$a_{\perp} [\text{au}]$	$0.681^{+0.102}_{-0.110}$
$D_L [\text{kpc}]$	$6.421^{+0.878}_{-0.991}$